Sexually dimorphic RNA helicases DDX3X and DDX3Y differentially regulate hollow condensates of DDX3X disease variants

Hui Shen[1,†], Michael C. Owens[1,2,†], Amber Yanas[1,2], Ellen Lavorando[1,2], Hsin-Yao Tang[3], and Kathy Fange Liu[1,2,4,*]

Affiliations:

[1]Department of Biochemistry and Biophysics, Perelman School of Medicine, University of Pennsylvania, Philadelphia, PA 19104, USA

[2]Graduate Group in Biochemistry and Molecular Biophysics, Perelman School of Medicine, University of Pennsylvania, Philadelphia, PA 19104, USA

[3]Molecular and Cellular Oncogenesis Program, The Wistar Institute, Philadelphia, PA 19104, USA

[4]Lead contact

[†]These authors contributed equally

*Correspondence: liufg@pennmedicine.upenn.edu

Abstract

The sex chromosome-encoded RNA helicases DDX3X and DDX3Y play important roles in RNA metabolism. Heterozygous mutations of DDX3X frequently occur in cancers and neurodevelopmental disorders which have strong sex biases. However, how different DDX3X variants impair cellular function in sex specific genetic background is not understood. Herein, we found that DDX3X variants with significantly impaired ATPase activities demixed into the shells of unique hollow condensates, the dynamics of which were further differentiated by the RNA binding affinities of the different DDX3X variants. Proteomic and imaging studies revealed that DDX3X variant condensates sequestered wild-type DDX3X, DDX3Y, and other proteins important for various signaling pathways. Intriguingly, wild-type DDX3X improved the dynamics of heterogenous variant/wild-type hollow condensates more than DDX3Y. These results suggest that DDX3X variants with distinct enzymatic and condensation propensities may interact uniquely with wild-type DDX3X or DDX3Y to cause sex-specific cellular impacts.

Keywords: DDX3X, DDX3Y, RNA helicase, disease variants, hollow condensates, ATPase activity, RNA binding

Main

The DEAD-box RNA helicase DDX3X is a crucial component of numerous cellular and developmental processes[1] that is conserved from yeast to humans[2]. Whole-body knockout of *Ddx3x* leads to embryonic lethality in mice[3], and knockdown of Ddx3x in the developing murine nervous system disrupts cortex development[4], highlighting the essential nature of DDX3X. DDX3X contains a helicase core common to all DEAD-box proteins that is flanked by two intrinsically disordered regions (IDRs) (**Fig. 1a**)[5]. The non-processive RNA unwinding activity of the helicase core helps DDX3X facilitate the translation initiation of specific transcripts via unwinding their highly structured 5' untranslated regions (5'UTRs) under unstressed conditions[6]. Upon cellular stress, the IDRs of DDX3X (particularly its N-terminal IDR) drive DDX3X to undergo liquid-liquid phase separation (LLPS) and participate in stress granule formation, which leads to translation repression[7].

Recent studies have reported over 100 recurrent mutations in DDX3X in numerous cancers including medulloblastoma[8–10], Burkitt's lymphoma[11], chronic lymphocytic leukemia and natural killer-T cell lymphoma[12–14]. Mutations in DDX3X are also linked to DDX3X syndrome, which accounts for 1-3% of otherwise unexplained intellectual disability cases[4]. These mutations often cause defects in the enzymatic activities (RNA unwinding, ATPase activity, and RNA binding), although the degree to which a mutation in DDX3X affects its enzymatic activities varies from disease variant to disease variant[4,10,15]. As a consequence of disrupting the catalytic activity, several variants of DDX3X are known to negatively impact translation[10], in particular the translation of known DDX3X targets[4]. Despite the fact that the majority of these mutations are in the catalytic core of DDX3X and not it its IDRs, disease variants of DDX3X frequently aberrantly phase separate in cells without addition of an external stressor[4,10]. This suggests that the enzymatic and phase separation properties of DDX3X are linked, although much work remains to decipher how the enzymatic and phase separation defects caused by different DDX3X variants contribute to the development of their related disorders.

The disorders associated with DDX3X variants, as well as a wide range of others, often manifest in a sex-biased manner. For example, DDX3X-related neurodevelopmental disorder (DDX3X syndrome) is significantly more common in XX individuals than in XY individuals[4], while XX indiviuals with pediatric medulloblastoma have a higher survival probability than XY individuals[16]. Recently, a growing body of evidence suggests that some of these sex biases may stem from the different biochemical and biophysical properties of sexually dimorphic protein homologs[17–20]. DDX3X and its Y chromosome-encoded homolog DDX3Y are two of these sexually dimorphic proteins. Because mutants of DDX3X are often heterozygous[21,22], the mutant allele will almost always be co-expressed with either wild-type (WT) DDX3X (in XX individuals) or with DDX3Y (in XY individuals). However, it is not known whether the enzymatic and condensation defects of DDX3X disease variants are differently altered by co-expression with WT DDX3X or DDX3Y.

Here, we focused on twelve DDX3X disease variants that span across the conserved helicase core of DDX3X for in-depth investigation of their enzymatic and condensation properties, cellular morphologies, and interactions with WT DDX3X and DDX3Y in cells. The results suggest that the ATPase deficiency of select DDX3X variants contributes to their demixing into a unique hollow condensate structure. We further identified the protein constituents of DDX3X hollow variant condensates, which included WT DDX3X, DDX3Y, and additional proteins important for various cell signaling pathways. Intriguingly, we found that WT DDX3X more strongly improved the dynamics of the variant condensates compared to WT DDX3Y, and that most hollow variants were more dynamic when co-condensed with WT DDX3X than with DDX3Y. These findings highlight different DDX3X variants having distinct condensation propensities to have sex-biased impacts in human disorders when functioning in the presence of WT DDX3X or DDX3Y in the sex-specific genetic background.

Results

DDX3X variants with decreased ATPase activities form cytoplasmic hollow puncta

Like other members of the DEAD-box family, the catalytic core of DDX3X consists of two RecA-like domains [amino acids (a.a.) 182 – 404 and 414 – 544] flanked by N- and C-terminal intrinsically disordered regions (IDRs) (a.a. 1 – 181 and 545 – 662). Within the two RecA-like domains are twelve conserved motifs that have been implicated in either binding and hydrolyzing ATP (Q, I, II, and VI motifs, in red), binding RNA (Ia, Ib, Ic, IV, IVa, and V motifs, in blue) or coordinating these functions (III and Va motifs, in green)[5] (**Fig. 1a**). In this study, we selected one disease mutation in (or near) each of these twelve conserved motifs to study how these mutations impair DDX3X's enzymatic activities and condensation properties.

To begin, we expressed either WT DDX3X or one of twelve disease variants (each tagged with mClover3) (**Fig. 1a**) to similar levels in HeLa cells (**Fig. 1b**). WT DDX3X showed diffuse localization throughout the cytoplasm in unstressed cells, which is consistent with previous studies[4,10,19] (**Fig. 1c**). Strikingly, five of the variants (G302V, G325E, R475G, A497V, and R534H) formed nearly perfectly spherical cytoplasmic puncta in which DDX3X was enriched in the outer shell but depleted in the center (**Fig. 1c and 1d**). This morphology was also observed in HEK293T cells (**Fig. 1e**), and orthogonal projections of one representative variant (R475G) further supported the unique hollow structure with the variant protein enriched in the shells (**Fig. 1f**). The percentages of cells with any hollow puncta varied among these five "hollow" variants; while four of these mutants formed hollow puncta in ~20% of cells, R475G formed hollow puncta in greater than 90% of cells (**Fig. 1g**). To control for possible differences in protein concentrations, we expressed R475G and WT DDX3X across a range of concentrations in HeLa cells. The results consistently showed that R475G, but not WT DDX3X, formed hollow puncta at all concentrations measured (**Fig. 1h and 1i**).

Four of the other variants used in this study (T275M, R351W, E449G, and L505V) were diffuse in the cytoplasm like WT DDX3X; these variants are hereafter referred to as "diffuse"

variants (**Extended Data Fig. 1a**). Additionally, we observed that the remaining three variants (T204P, A222P, and S382R) presented with small and solid foci with irregular shape throughout the cytoplasm; these variants are hereafter referred to as “speckled” variants (**Extended Data Fig. 1a**). The speckled variants precipitated to the cell pellet after lysis of HeLa cells using radioimmunoprecipitation assay (RIPA) buffer (**Extended Data Fig. 1b**). These data suggest that these three variants may impact protein folding.

Upon cellular stress, WT DDX3X undergoes LLPS and joins stress granules (SGs)[7]. This led us to question whether the hollow puncta we observed were, in fact, SGs. Under unstressed conditions, none of the variant’s puncta colocalized with the canonical SG marker G3BP1[23] (**Fig. 1c and 1d**). Upon arsenite treatment, most of the DDX3X variants colocalized with G3BP1, suggesting that they entered SGs, except for the speckled variants (**Extended Data Fig. 1c**). Collectively, these results suggest that DDX3X variants have distinct cellular condensation propensities, expression patterns, and possibly different protein interactomes compared to WT DDX3X under stressed and unstressed conditions.

As the ATPase activity of DEAD-box enzymes often influence their condensation properties[24], we assayed the ATP hydrolysis activity of these variants. mCherry-tagged WT and variant DDX3X were purified to near homogeneity and subjected to a malachite green ATPase assay as previously described[19] (**Fig. 1j and Extended Data Fig. 1d**). While we were able to express and purify the diffuse and hollow variants, we were unable to express and purify the three speckled variants in our bacterial expression system, in line with our previous observation that these variants may be misfolding. All the hollow variants exhibited significantly lower ATPase activities than the diffuse variants and WT DDX3X, suggesting that ATPase activity may correlate with their propensity to form hollow condensates in cells. Given that ATP hydrolysis is necessary for the release of bound RNAs[15,25–27], it is possible that the unreleased RNA functions as a multivalent platform that recruits additional DDX3X molecules and other proteins, contributing to hollow puncta formation. Our data point towards a model in which mutations in DDX3X that greatly

impair its ATPase activity drive the formation of hollow cytoplasmic puncta that are unique from SGs.

RNA binding affinity influences inter- and intramolecular dynamics of DDX3X variant hollow condensates

Unlike WT-DDX3X which only undergoes liquid-liquid phase separation under stressed conditions[7], select DDX3X variants have increased phase separation propensities leading to condensate formation under unstressed conditions[4,10]. A key trait of liquid-liquid phase separated condensates is that they are in a dynamic equilibrium with their surroundings[28]. To directly study the molecular exchange between the cytoplasm and the hollow condensates formed by DDX3X variants, we performed "full bleach" fluorescence recovery after photobleaching (FRAP) experiments, in which we bleached an entire hollow condensate and measured the time-resolved fluorescence signal recovery (**Extended Data Fig. 2a**, left). We found that the fluorescence of G302V, G325E, A497V, and R534H hollow condensates recovered gradually, while the fluorescence of R475G hollow condensates barely recovered in the same timeframe (**Fig. 2a**, left **and 2b**, top). Additionally, "partial bleach" experiments were carried out to reveal the mobility of molecules within the hollow condensates (**Extended Data Fig. 2a**, right)[29]. Similarly, the fluorescence of R475G hollow condensates showed no recovery after partial bleaching unlike the other variants, consistent with the full bleach results (**Fig. 2a**, right **and 2b**, bottom). The lower inter- and intramolecular dynamics of the R475G hollow condensates sets them apart from the other variant hollow condensates. The distinct dynamic activity of the R475G variant is in line with our previous finding that the percentage of cells expressing hollow condensates was much higher for R475G than for the other variants (**Fig. 1g**).

Previous studies suggest that RNA binding deficiencies of RNA binding proteins such as FUS (fused in sarcoma) decreased the dynamics of the protein-RNA condensates[30]. Thus, we compared the RNA binding capabilities of WT and DDX3X variants. We performed electrophoretic

mobility shift assays (EMSAs) using a fluorescently-labeled double-stranded RNA probe that has been previously described to be bound by DDX3X[19,31]. While all the hollow variants displayed weaker RNA binding affinity than WT DDX3X, R475G had the weakest RNA binding affinity (**Fig. 2c and Extended Data Fig. 2b**). This suggests that the decreased RNA binding capacity of R475G may decrease the dynamics of its hollow condensates relative to the other hollow variants.

Furthermore, to assess whether the decreased RNA binding affinities measured *in vitro* correspond to decreased RNA binding in cells, we utilized click chemistry to fluorescently label nascent RNA in HeLa cells after incorporation of 5-ethynyluridine (5-EU) (**Extended Data Fig. 2c**). The results showed that the cytoplasmic RNAs were enriched in the outer shells of hollow condensates relative to the cytoplasm and the center of the condensates (**Fig. 2d**). After quantifying the RNA signal intensity in the condensates' shells of each of the hollow variants (normalizing to the RNA signal in the nucleoplasm), we found that R475G hollow condensates had the weakest 5-EU signals of all the tested variants, consistent with the *in vitro* EMSA data (**Fig. 2e**).

Iterative mutations at the Arg475 position further support roles of the ATPase activity and RNA binding affinity in hollow condensate formation and dynamics

Our findings suggest that the formation of hollow condensates is correlated with a reduction in these variant's ATPase activities (**Fig. 1j**) and that once formed, the dynamics of these hollow condensates is influenced by their RNA binding capabilities (**Fig. 2c and 2e**). To further investigate these correlations, we focused on the Arg475 residue of DDX3X, as the R475G variant showed the strongest propensity to form hollow condensates in cells (**Fig. 1d and 1g**). We performed single-site mutagenesis and developed the following variants at amino acid Arg475: R475A (small and uncharged, like the disease implicated glycine variant) and R475K (positively charged, similar to the original arginine) (**Fig. 3a**). First, we expressed these variants (mClover3-tagged) to similar levels in HeLa cells (**Extended Data Fig. 3a**) and performed fluorescence

imaging. R475G and R475A both formed hollow condensates, whereas R475K was diffuse in the cytoplasm, like WT DDX3X (**Fig. 3b**). Like the other variants tested (**Fig. 1c and 1d**), G3BP1 was not present in R475A hollow puncta under unstressed conditions (**Fig. 3b**). Upon arsenite treatment, R475A, R475G, and R475K all entered G3BP1-positive SGs (**Extended Data Fig. 3b**). Next, we purified mCherry-tagged constructs of these iterative variants (**Extended Data Fig. 3c**) and repeated the ATPase assay. Relative to WT DDX3X, R475A and R475G showed less than 15% ATPase activity, while R475K showed ATPase activity much closer (85%) to WT DDX3X (**Fig. 3c**). This supports our model that a significant deficit in ATPase activity drives formation of hollow condensates. Additionally, we quantified the RNA binding ability and condensate dynamics of R475A and R475K. The EMSA results showed that R475G and R475A both had severe defects in RNA binding affinity in comparison to WT DDX3X and R475K (**Fig. 3d and Extended Data Fig. 3d**). In line with this, the full and partial bleach FRAP results showed that R475A condensates had significantly decreased recovery dynamics, similar to R475G (**Figs. 2a and 3e**), reinforcing that reduced RNA binding ability may contribute to the reduced dynamics of the hollow condensates.

R475G hollow condensates enrich proteins in various signaling pathways and deplete translation machinery

Under unstressed conditions, DDX3X variant hollow condensates lack the SG marker protein G3BP1, indicating that these condensates are not SGs (**Fig. 1c**). This raised the possibility that these condensates may sequester unique proteins and have functions divergent from those of SGs. To understand the potential biological functions of these hollow condensates, we sought to identify their protein components using an adapted ascorbate peroxidase (APEX2)-based proximity labeling method[32–34] (**Fig. 4a**). The labeling efficiency and specificity of APEX2-tagged DDX3X were examined as previously shown[19]. In this study, we prioritized comparing the protein

networks of R475G and WT DDX3X, as R475G displayed the highest propensity to form hollow condensates among all the variants tested.

APEX2-WT-DDX3X and APEX2-R475G were expressed in cells at a similar level (**Extended Data Fig. 4a**). After incubating with biotin-phenol for 30 min, cells were exposed to H_2O_2 for 1 min to trigger biotin labelling by the APEX2 moiety. Cells were then lysed, and the labeled proteins were enriched via streptavidin pulldown. Protein labeling and enrichment were analyzed by western blots before being subjected to proteomics analysis (**Extended Data Fig. 4b**). The western blots and Coomassie stain results showed that the biotinylated proteins were enriched in pulldown fractions compared to the flowthrough and the input samples (**Extended Data Fig. 4b**).

Unsupervised hierarchical clustering of the APEX2-MS protein abundances resulted in two separate clusters for the biological triplicates of APEX2-WT and APEX2-R475G, indicating that R475G mutation was the main determinant of differences between the interactomes (**Extended Data Fig. 4c**). Proteins with significantly altered abundance were selected based on the following criteria: (1) minimum fold-change of 2 in either direction, adjusted p-value < 0.1, (2) identified by a minimum of 2 peptides, and (3) detected in at least two replicates (**Supplementary Table1**).

Analysis of these significant proteins revealed that, compared to the APEX2-WT-DDX3X pulldown, 33 proteins were enriched in APEX2-R475G hollow condensates while 128 proteins were depleted (**Fig. 4b**). Gene Ontology analysis suggests that the proteins enriched in R475G condensates participate in the regulation of Rac protein signal transduction and protein polymerization, while proteins depleted in R475G condensates mainly play roles in translation regulation and ribonucleoprotein complex biogenesis (**Fig. 4c and 4d**).

Because these hollow condensates appear biphasic, with the potential for proteins to either accumulate in the hollow core or the spherical shell of the puncta, we next sought to determine where in the condensates the proteins identified in our proteomics screen might reside.

In a previous study of TDP-43 hollow condensates, it was determined that conventional antibody-based immunofluorescence cannot be used to detect the components in the hollow core, as fixation produces a barrier that prevents antibody penetration[35]. Thus, TRIM32 (an E3 ubiquitin ligase) and ANKRN52 (a regulatory protein of protein phosphatase 6), two top targets enriched in APEX2-R475G mass spec pulldown (**Fig. 4b**), were constructed with an mCherry tag, and then subjected to fluorescence imaging. In WT DDX3X-expressing cells, TRIM32 and ANKRN52 were mostly diffuse in the cytoplasm, with TRIM32 showing small foci. In contrast, in cells expressing R475G, TRIM32 and ANKRD52 were sequestered inside of R475G hollow condensates (**Fig. 4e**) in a pattern similar to R475G. The trapping of these proteins in the relatively undynamic condensates of R475G may disrupt the cellular pathways in which they normally participate.

DDX3X variant hollow condensates recruit WT DDX3X and DDX3Y

As the vast majority of DDX3X disease variants are expressed heterozygously[4,36], we wondered whether DDX3X disease-related variants co-condense with WT DDX3X or DDX3Y in cells. To test this, we first co-expressed mCherry-tagged WT DDX3X with each of the mClover3-tagged hollow mutants at a similar expression level in HeLa cells to look for the presence of co-condensates. When co-expressed, WT DDX3X was recruited to the shells of all the hollow condensates formed by each variant (**Extended Data Fig. 5a**). The presence of these co-condensates without addition of a stressor suggests that these DDX3X variants could contribute to disease (at least partially) by trapping WT DDX3X within their hollow condensates. To assess the ability of WT DDX3X molecules to move between the hollow condensates and the cytoplasm, we measured the dynamics of WT DDX3X sequestered in the hollow condensates using full bleach FRAP experiments. WT DDX3X recovered to ~80% of its original intensity when its co-condensates with G302V, G325E, A497V, and R534H, however, WT DDX3X only recovered to ~40% of its original intensity when in co-condensates with R475G (**Fig. 5a and 5c**, left). While all

the hollow variant condensates interfere with the cellular localization of WT DDX3X, condensates of R475G appeared to trap WT more strongly than other variants.

We next repeated these experiments with DDX3Y and the hollow DDX3X variants. Co-expression of mCherry-tagged DDX3Y and each of the mClover3-tagged DDX3X variants showed that, as with WT DDX3X, DDX3Y was recruited to the shells of each variant's hollow condensate (**Extended Data Fig. 5b**). In our previous work, we found that condensates of DDX3Y (both *in vitro* and in cells) were less dynamic than condensates of DDX3X[19]. We wondered whether the same would be true for DDX3Y in co-condensates with DDX3X variants. Thus, we repeated the full bleach FRAP in HeLa cells co-expressing DDX3Y and each of the DDX3X variants. (**Fig. 5b and 5c**, right). The results with DDX3Y largely mirrored those with WT DDX3X: the sequestered DDX3Y in the G302V, G325E, A497V, and R534H condensates was more dynamic than in R475G condensates (**Fig. 5c**). However, WT DDX3Y only recovered to ~60% of its original intensity when sequestered in G302V, G325E, A497V, and R534H hollow condensates, and ~20% when sequestered into R475G condensates. The mobile fraction of DDX3Y was significantly lower than the mobile fraction of WT DDX3X in each type of co-condensate measured (**Fig. 5d**), although there was no significant difference in recovery halftime for G302V and R475A variants when co-condensate with either DDX3X or DDX3Y (**Extended Data Fig. 5c**). The reduced dynamics of these co-condensates suggests that sequestration of WT DDX3X or DDX3Y within hollow condensates may inhibit their ability to facilitate translation, as both WT DDX3X and DDX3Y participate in translation initiation[37].

WT DDX3X more strongly increases the dynamics of the variant condensates than WT DDX3Y

Reciprocally, we performed full bleach FRAP on DDX3X hollow variants in co-condensates with WT DDX3X or DDX3Y. When co-expressed with mCherry-tagged WT DDX3X

(**Fig. 6a and 6b**), all the hollow variants showed improved mobile fractions (**Extended Data Fig. 6a**) compared to when they are expressed alone (**Fig. 6e and 6f**), although the magnitude of this effect was much smaller for R475G than it was for the other hollow variants. However, when co-expressed with mCherry-tagged DDX3Y (**Fig. 6c and 6d**), only G325E showed significant improvement in its mobile fraction. Additionally, both DDX3X and DDX3Y were able to reduce the recovery halftime for all the hollow variants except for R475G (**Extended Data Fig. 6b**). These data indicate that co-condensates of WT DDX3X and variant DDX3X (which would be present in XX individuals with a mutated *DDX3X* allele) are more dynamic than co-condensates of DDX3Y and variant DDX3X (which would be present in XY individuals with a mutated *DDX3X* allele).

Discussion

Select DDX3X variants form unique cytoplasmic hollow condensates in cells

The formation of membraneless compartments within cells via liquid-liquid phase separation is crucial for the proper regulation of several cellular processes, ranging from gene expression to signal transduction[38,39]. Some condensates have a uniform spherical morphology in which each component is fairly well-distributed, such as SGs[40], while others have distinct sub-compartments, such as the nucleolus [41]. In addition, a different class of multilayered condensates has been reported where the condensate forms a vesicle-like structure with a seemingly hollow internal space[29,35,42]. Until this point, these hollow cellular condensates have only been observed in the nucleus when seen in cells[35]. In our current study, we found that several disease variants of DDX3X can form hollow condensates in the cytoplasm (**Fig. 1**).

Formation of these hollow condensates can either be a passive process regulated by the protein's own biochemical and/or biophysical properties or be an active process driven by "chaperone" proteins[35]. In the case of *in vitro* condensates of protamine, hollow condensates are formed via the liquid-liquid phase separation of protein-RNA complexes when the RNA:protein ratio was either >1.87 or <0.075[42]. On the other hand, RNA binding-deficient mutants of TDP-43 require the ATPase activity of HSP70 to form hollow condensates[35]. For the DDX3X variants tested in this study, we found that the propensity to form hollow condensates was correlated with the proteins' decreased ATPase activities (**Fig. 1**), and that the dynamics of these hollow condensates may be linked to their RNA binding affinities (**Fig. 2**). Via our APEX2-MS analysis, we did not find any chaperone-like proteins inside of the hollow condensate, suggesting a mechanism of formation more akin to protamine than to TDP-43 (**Fig. 4**).

Hollow condensates of DDX3X variants may exert their disease effects via sequestration of other proteins

Under unstressed conditions, WT DDX3X is diffuse in cells, whereas upon addition of stressors such as oxidative stress or energy depletion, it is compartmented into G3BP1-positive SGs[7]. In contrast, the five hollow variants identified herein formed their cellular condensates without addition of an external stressor. These hollow condensates do not contain G3BP1, meaning that they are not "canonical" SGs[40]. This raised the question as to what role these hollow condensates play in disease. To address this question, we performed APEX2 proximity labeling followed by mass spectrometry to identify the other protein components of hollow condensates formed by DDX3X R475G (**Fig. 4**). Our APEX2-MS results revealed that R475G hollow condensates sequestered a subset of proteins that do not interact with WT DDX3X. In particular, R475G condensates are depleted of proteins relating to protein translation, further separating them from SGs[40].

One of the most enriched proteins in R475G condensates was the E3 ubiquitin ligase TRIM32. During neuronal development, TRIM32 drives neural progenitor differentiation by preferentially accumulating in one daughter cell during division. The TRIM32-positive daughter cell will differentiate into a mature neuron, while the TRIM32-negative daughter cell will remain a progenitor[43]. Expression of R475G in neural progenitor cells might disrupt the proper segregation of TRIM32, as its hollow condensates are significantly less dynamic than condensates of other variants (**Figs. 2 and 5**). This possibly contributes to R475G's more severe neurodevelopmental phenotypes than some other DDX3X variants[4]. In addition to TRIM32, many of the other proteins enriched in R475G condensates were involved in the regulation of Rac signaling. DDX3X variants may thus also dysregulate Rac signaling, which has been implicated in a number of cancers[44]. The disease implications of these sequestered proteins warrant further investigation on the potential pathological links.

The distinct condensation properties of DDX3X variant hollow condensates may correlate with sex biases in disease incidence and severity

Beyond the protein components identified in our APEX2-MS screen, fluorescence imaging revealed that DDX3X variant hollow condensates sequestered WT DDX3X or DDX3Y when co-expressed in cells (**Extended Data Fig. 5**). FRAP experiments further revealed that co-condensates of variant DDX3X and WT DDX3X were more dynamic than co-condensates of variant DDX3X and WT DDX3Y (**Figs. 5 and 6**). These differing condensation properties may contribute to the sex biases in incidence and severity of DDX3X-related disorders[4,16]. Based on our results, we hypothesize that DDX3X variant hollow condensates formed in XY individuals would be less dynamic and more able to sequester the remaining DDX3Y (and other constituent proteins) than condensates formed in XX individuals. Future work should prioritize the study of these mutants in both XX and XY chromosomal sex-defined genetic backgrounds. Collectively, the results of this study indicate that the enzymatic properties of select DDX3X disease variants contribute to the formation of cytoplasmic hollow condensates with unique protein components which may contribute to sex bias in human disorders.

AUTHOR CONTRIBUTIONS

H.S., M.C.O. and K.F.L. designed the experiments. H.S., A.Y., M.C.O., and E.L. generated the constructs and the mammalian cell lines used in this study. H.S., A.Y., M.C.O., and E.L. purified the recombinant DDX3X and DDX3X variants used in this study. H.S. and A.Y. performed the immunofluorescence imaging and FRAP experiments and analyzed the data. M.C.O., and E.L. performed the EMSA and ATPase activity assays. H.S. performed the APEX2 proteomics and H.Y.T performed the proteomic data analysis. All authors participated in writing, discussing, and editing the manuscript.

DECLARATION of INTEREST

The authors declare no competing interests.

DATA AVAILABILITY

Any data supporting the findings of this study and additional information required to reanalyze the data reported in this paper is available from the lead contact upon request.

ACKNOWLEDGEMENTS

This work was supported by the National Institutes of Health (R35GM133721 and R01HL160726 to K.F.L., R35GM133721-03S1 to A.Y., R50CA221838 to H.Y.T, and T32GM132039 to M.C.O.). K.F.L. is supported by the American Cancer Society (RSG-22-064-01-RMC). We thank Dr. Matthew Kayser for sharing the Leica SP8 confocal microscope. We would also like to thank Drs. Matthew Weitzman and Roger Greenberg for their helpful comments while drafting this manuscript. Fig. 1a was created with Biorender.com.

Figures and figure legends

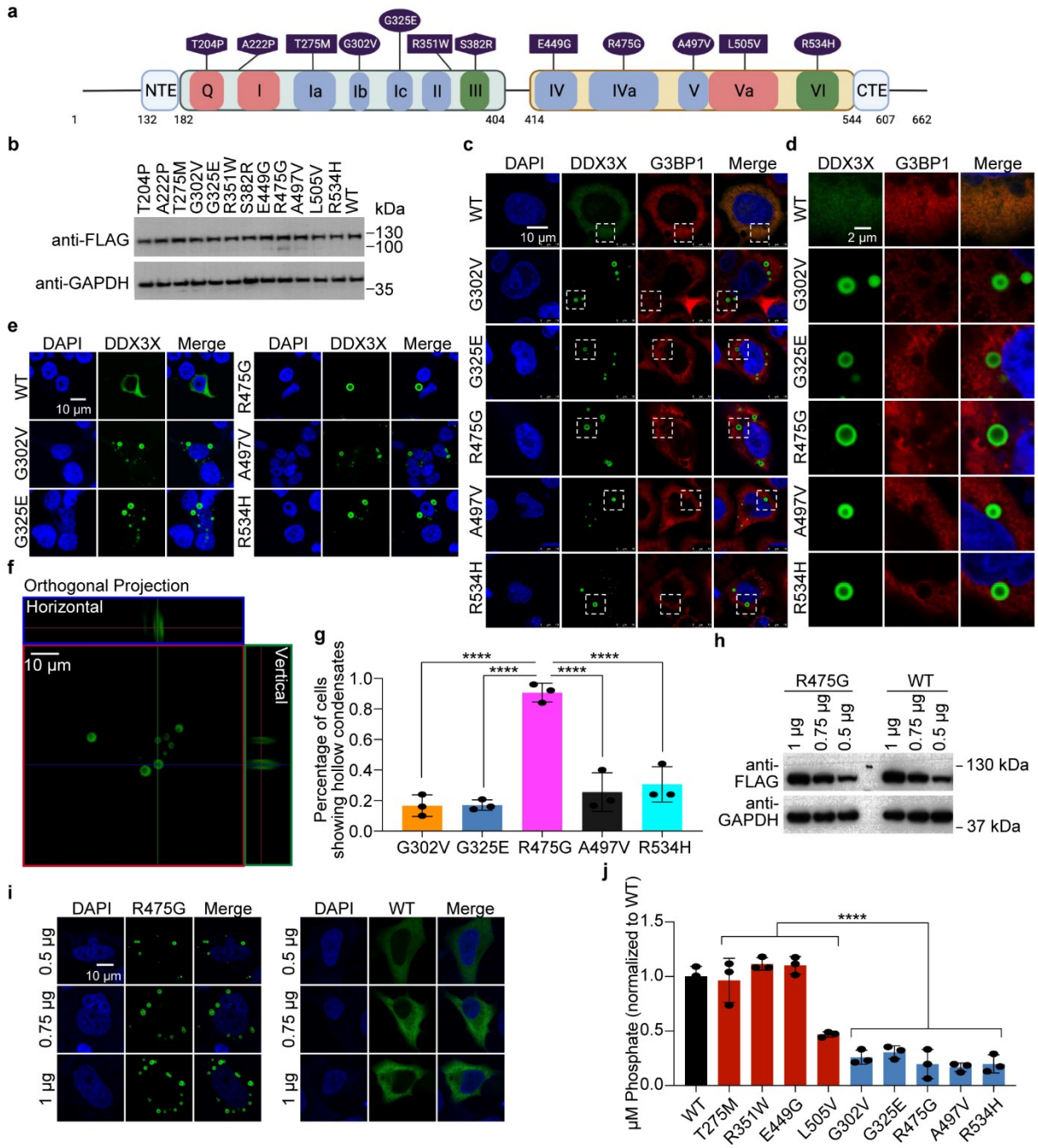

Fig. 1: DDX3X variants with decreased ATPase activities form hollow puncta in cells.

a, Schematic of the conserved domains and motifs of DDX3X and the locations of each disease variant used in this study. Motifs responsible for ATP binding and hydrolysis are in red, RNA binding in blue, and coordination of ATPase and RNA binding in green. Diffuse variants are shown

in squares, speckled are shown in hexagons, and hollow mutants are shown in ovals. **b**, Western blots showing that the mClover3-tagged DDX3X variants were expressed at similar levels in HeLa cells. **c**, Representative images showing the localization of mClover3-tagged WT DDX3X or the indicated variants and mCherry-tagged G3BP1 in HeLa cells. The white boxes indicate regions zoomed in **d**. Scale bar, 10 μm. **d**, Zoomed-in view of hollow condensates formed by the indicated DDX3X variants in **c**, showing that these hollow condensates do not colocalize with the stress granule marker G3BP1. **e**, Representative images of cellular distributions of the mClover3-tagged DDX3X variants in HEK293T cells. Scale bar, 10 μm. **f**, Orthogonal projections demonstrating that mClover3-tagged R475G forms puncta in which it is enriched in the spherical shell but de-enriched in the (seemingly) hollow core. Scale bar, 10 μm. **g**, Quantified percentage of transfected HeLa cells containing DDX3X variant hollow condensates. Values represent means ± s.d. from three independent measurements of 25 cells each. Significance was calculated using a two-tailed t-test. ****p <0.0001. **h**, Western blots showing comparable expression of mClover3-tagged WT and R475G DDX3X in HeLa cells after transfection with the three indicated plasmid concentrations. **i**, Representative images of mClover3-tagged WT DDX3X or R475G in HeLa cells transfected at the three indicated plasmid concentrations as in **h**. mClover-tagged R475G formed hollow puncta at all three concentrations while WT DDX3X remained diffuse. Scale bar, 10 μm. **j**, Malachite green ATPase activity assay of WT and DDX3X variants, as measured by release of free phosphate. Values were expressed in μM phosphate and normalized to the WT value. The background value (release of free phosphate when no RNA was added) was subtracted from each point before plotting, as described in methods. Values represent means ± s.d. from three independent replicates. Significance was calculated using a two-way ANOVA test. ****p <0.0001.

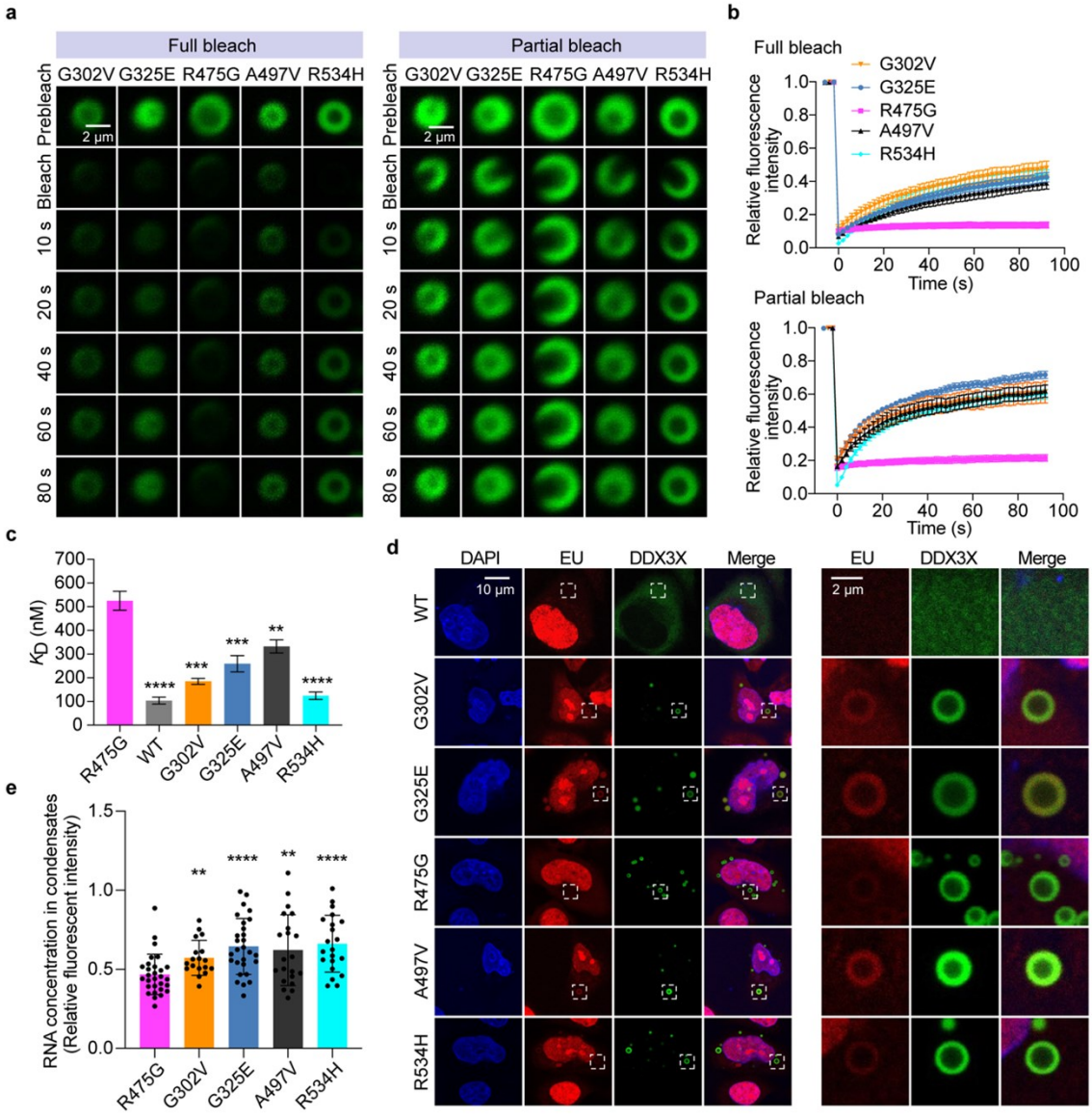

Fig. 2: RNA binding affinities impact the inter- and intramolecular dynamics of DDX3X variant hollow condensates.

a, Time-lapsed images of representative FRAP experiments on hollow condensates of the indicated mClover3-tagged DDX3X variants expressed in HeLa cells. Full bleach (left) and partial bleached (right) experiments were performed to measure the inter- and intramolecular dynamics (respectively) of each condensate. Scale bar, 2 µm. **b**, Recovery curves for the indicated mClover3-tagged DDX3X variants in HeLa cells. Top: recovery plot for full bleach experiments. Bottom: recovery plot for partial bleach experiments. The traces of the FRAP data represent

means ± s.e.m. from at least three biologically independent experiments. **c**, RNA binding affinities of WT and DDX3X hollow variants, were determined using EMSA. Values represent means ± s.d. from three independent experiments. Significance was calculated between R475G and each of the other variants using a two-tailed t test. $^{**}p < 0.01$; $^{***}p < 0.001$; $^{****}p < 0.0001$. **d**, Left: imaging of EU-labeled RNAs (red) in HeLa cells expressing mClover3-tagged WT or DDX3X hollow variants. Scale bar, 10 μm. Right: zoomed-in view of the boxed area from the left figures. Scale bar, 2 μm. **e**, Quantification of EU fluorescence intensity for each of the hollow condensates represented in **d**. Values were normalized using the fluorescence intensity in the nucleoplasm of each cell. Values represent means ± s.d. from 20 cells. Significance was calculated between R475G and each of the other variants using a two-tailed t test. $^{**}p < 0.01$; $^{****}p < 0.0001$.

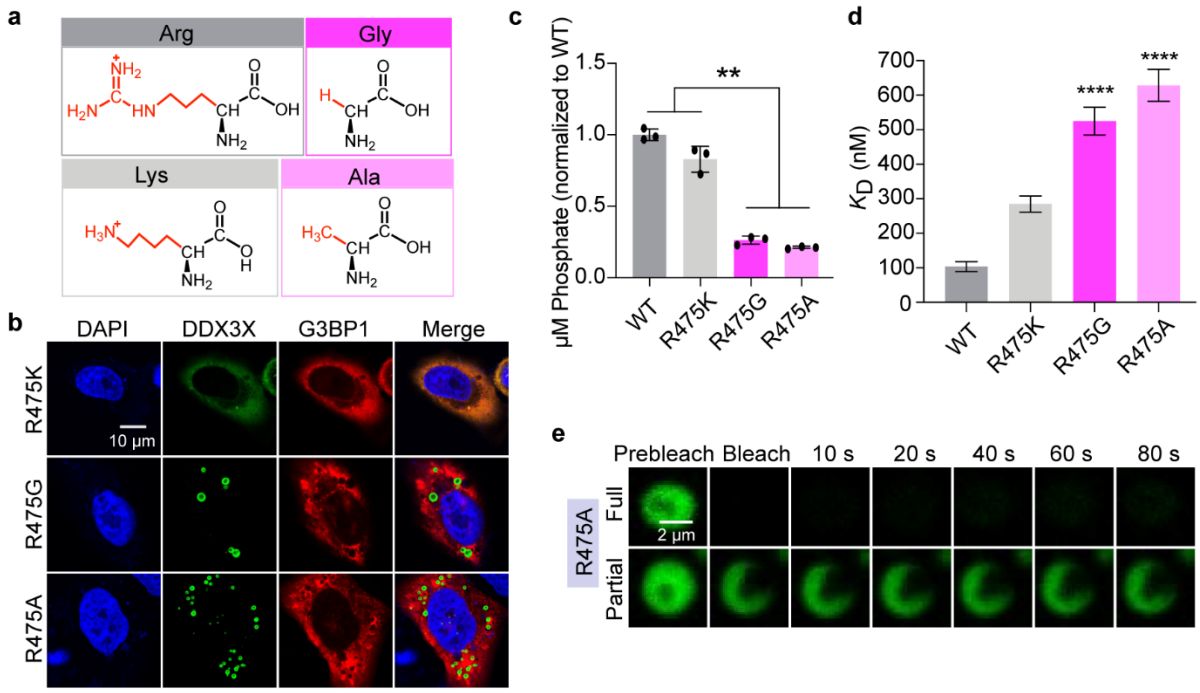

Fig. 3: Iterative mutations at the Arg475 position further support a role for ATPase activity and RNA binding in hollow condensate formation and dynamics.

a, Structures of amino acids described in these experiments. **b**, Representative images of the indicated mClover3-tagged DDX3X construct and mCherry-tagged G3BP1 expressed in HeLa cells. Scale bar, 10 µm. **c**, ATPase activities of mCherry-tagged WT, R475K, R475G, and R475A DDX3X, measured as in **Fig. 1j**. Values represent means ± s.d. from three independent replicates. Significance was calculated using a two-way ANOVA. ***p* <0.001. **d**, RNA-binding affinities of WT, R475K, R475G and R475A DDX3X, determined using EMSA, measured as in **Fig. 2c**. Values represent means ± s.d. from three independent experiments. Significance was calculated between WT and the others individually using a two-tailed t test. ****p <0.0001. **e**, Time-lapsed images of full bleached and partial bleached mClover3-tagged R475A condensates in HeLa cells. Scale bar, 2 µm.

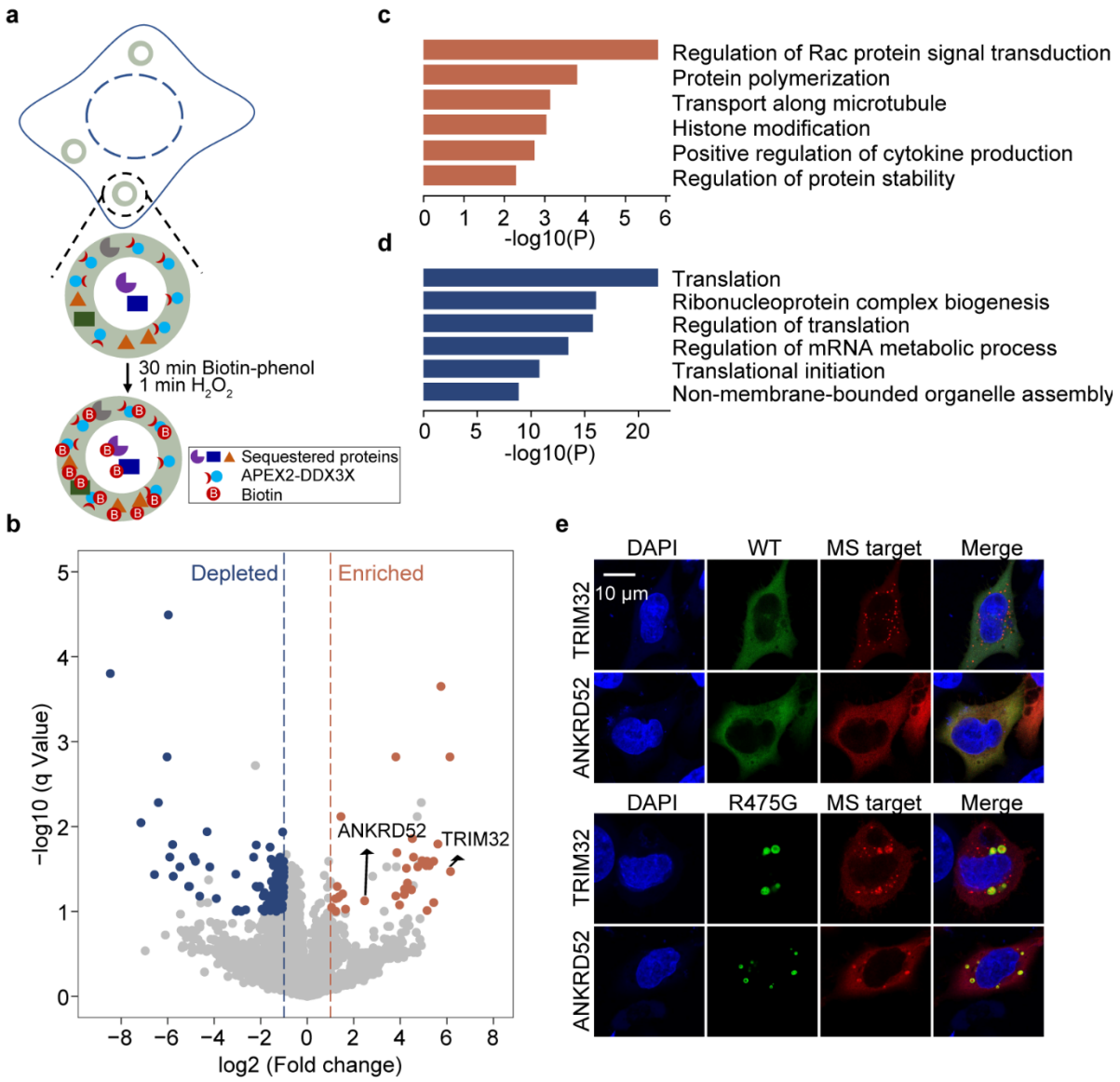

Fig. 4: R475G hollow condensates enrich proteins in various signaling pathways and deplete translation machinery.

a, Schematic of APEX2-mediated proximity labeling of proteins in R475G hollow condensates. **b**, Volcano plots showing differential protein enrichment via streptavidin pull-downs from APEX2-R475G compared to APEX2-WT expressing cells. Differentially enriched proteins are shown in orange (adjusted *p*-value < 0.1, $\log_2$ fold change > 1) and differentially depleted proteins are shown in blue (adjusted *p*-value < 0.1, $\log_2$ fold change < -1). The rest of the proteins are shown

in light gray. **c**, Gene Ontology (GO) analysis of the differentially enriched proteins in R475G condensates, illustrated as orange dots in **b**. **d**, Gene Ontology (GO) analysis of the differentially depleted proteins in R475G condensates, illustrated as blue dots in **b**. **e**, Representative images of localization of mCherry-tagged TRIM32 and ANKRN52 in mClover3-tagged WT- or R475G-expressing HeLa cells. Scale bar, 10 μm.

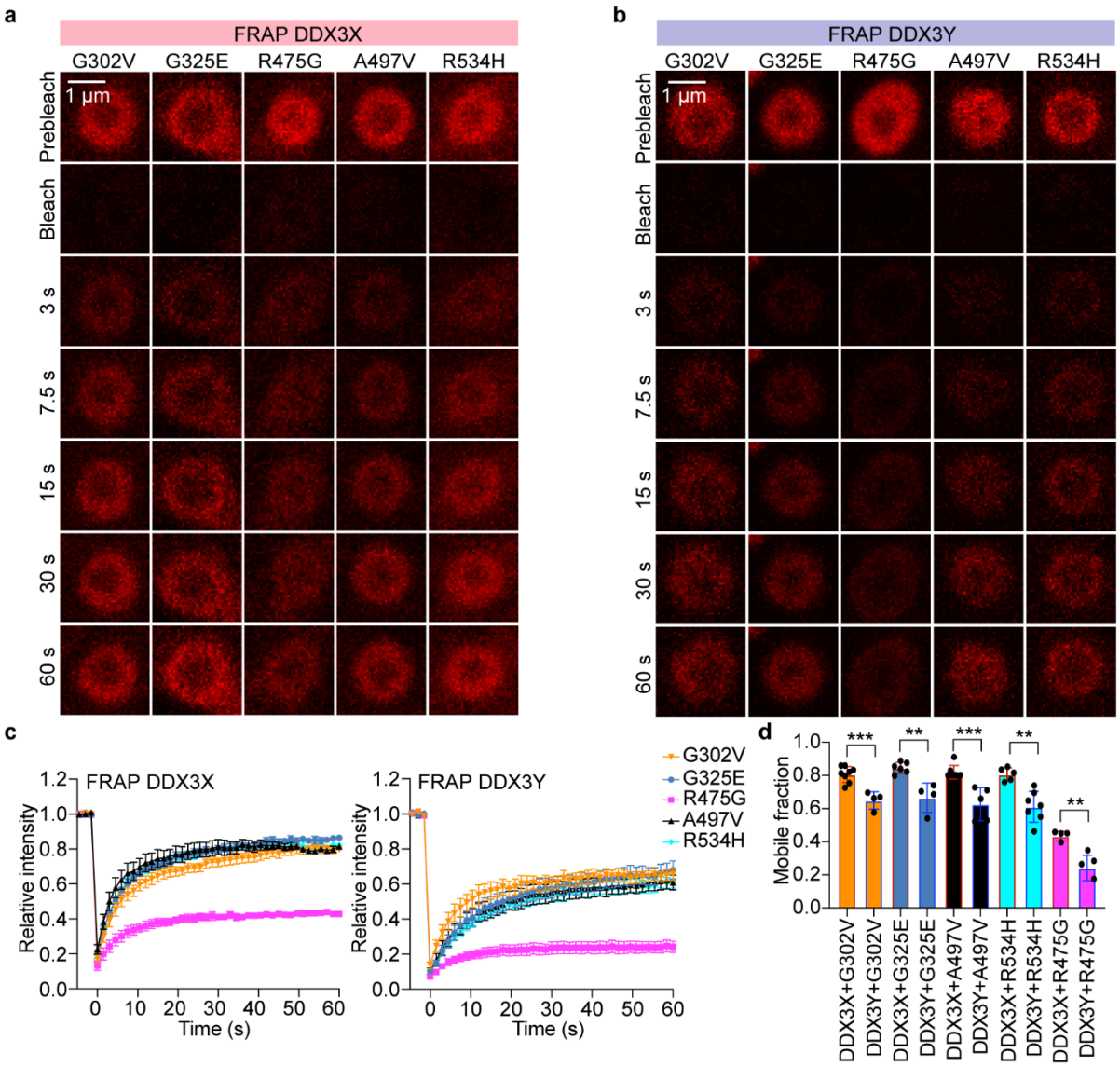

Fig. 5: DDX3X variant hollow condensates recruit WT DDX3X and DDX3Y.

a, Time-lapsed images of photobleached mCherry-tagged WT DDX3X trapped in the cytoplasmic hollow condensates formed by mClover3-tagged DDX3X hollow variants in HeLa cells from the cellular FRAP experiments. Scale bar, 1 μm. **b**, Time-lapsed images of photobleached mCherry-tagged WT DDX3Y trapped in the cytoplasmic hollow condensates formed by mClover3-tagged DDX3X hollow variants from the cellular FRAP experiments. Scale bar, 1 μm. **c**, Recovery curves for WT DDX3X (left panel) and DDX3Y (right panel) sequestered in the hollow condensates formed by mClover3-tagged DDX3X hollow variants in HeLa cells. The traces of the FRAP data

represent means ± s.e.m. from at least three biologically independent experiments. **d**, Comparison of the mobile fractions of mCherry-tagged WT DDX3X or DDX3Y in condensates with mClover3-tagged DDX3X variants, taken from the FRAP analysis in **c**. Mobile fraction was calculated as described in methods. Values represent means ± from at least three biologically independent experiments. Significance was calculated using a two-tailed t test. $^{**}p<0.01$; $^{***}p<0.001$.

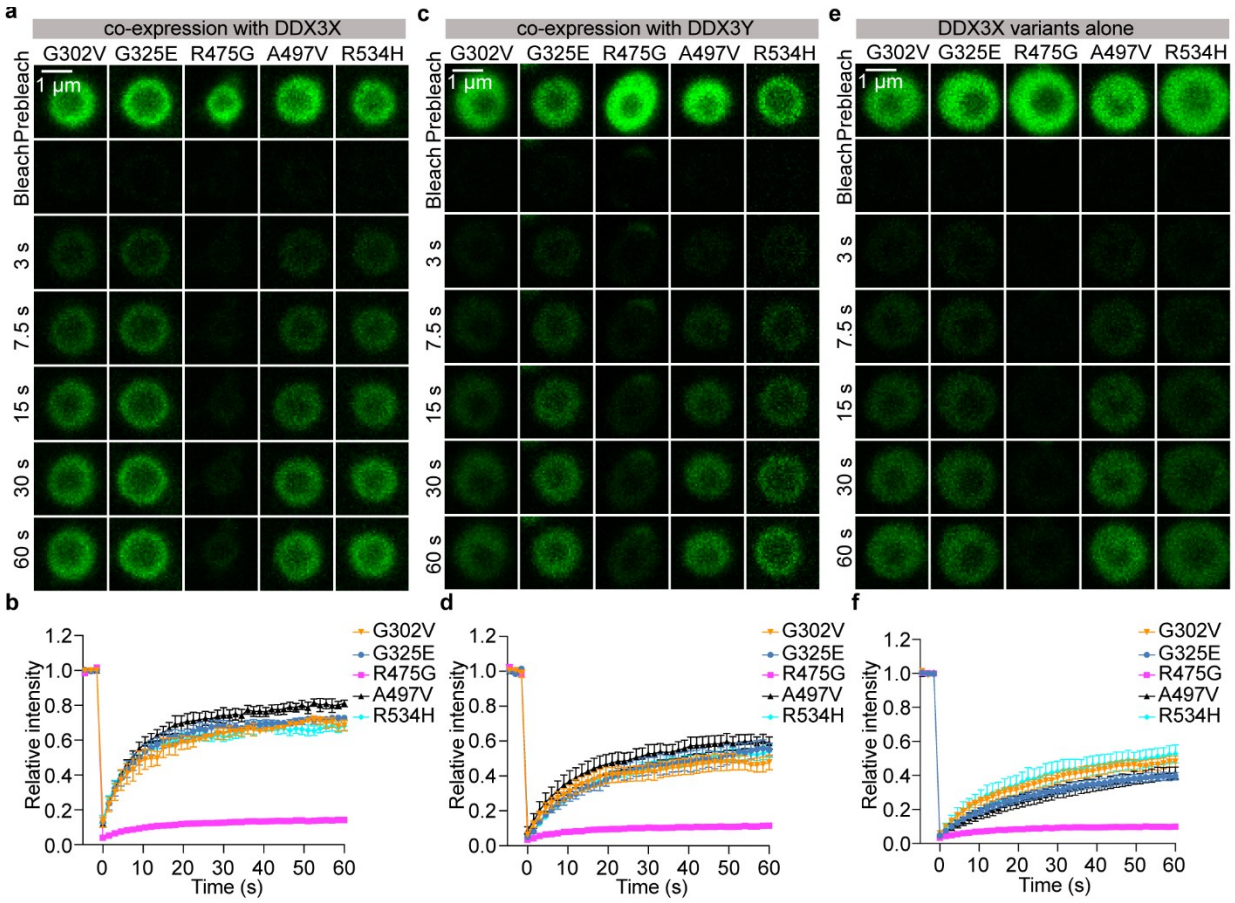

Fig. 6: Hollow variants of DDX3X, except for R475G, are more dynamic when co-condensed with WT DDX3X than with DDX3Y.

a, Time-lapsed images of photobleached mClover3-tagged variant DDX3X in the cytoplasmic hollow co-condensates with mCherry-tagged WT DDX3X in HeLa cells from the cellular FRAP experiments. Scale bar, 1 μm. **b**, Recovery curves for each mClover3-tagged DDX3X variant in hollow co-condensates with mCherry-tagged WT DDX3X in HeLa cells from the cellular FRAP experiments. The traces of the FRAP data represents means ± s.e.m. from at least three biologically independent experiments. **c**, Time-lapsed images of photobleached mClover3-tagged variant DDX3X in the cytoplasmic hollow co-condensates with mCherry-tagged DDX3Y in HeLa cells from the cellular FRAP experiments. Scale bar, 1 μm. **d**, Recovery curves for each mClover3-tagged DDX3X variant in hollow co-condensates with mCherry-tagged DDX3Y in HeLa

cells from the cellular FRAP experiments. The traces of the FRAP data represents means ± s.e.m. from at least three biologically independent experiments. **e**, Time-lapsed images of photobleached mClover3-tagged variant DDX3X in the cytoplasmic hollow condensates when expressed alone in HeLa cells from the cellular FRAP experiments. Scale bar, 1 μm. **f**, Recovery curves for each mClover3-tagged DDX3X variant in condensates when expressed alone in HeLa cells from the cellular FRAP experiments. The traces of the FRAP data represents means ± s.e.m. from at least three biologically independent experiments.

Methods

Cell culture, transfection, and *Escherichia coli* strains

HeLa and HEK293T cells were cultured in DMEM + GlutaMAX (GIBCO) with 10% FBS (GIBCO) and 1% Pen/Strep (Corning) in a humidified incubator with 5% CO_2 at 37°C. Lipofectamine 2000 (Invitrogen) was used for plasmids transfection. Experiments were conducted on transfected cells after 24 hrs transfection. For bacterial cell culture, TOP10 and BL21(DE3)-RIL chemically competent bacterial strains were grown in lysogeny broth containing the corresponding antibiotics at 200 rpm, 37°C.

Constructs

The DDX3X-mCherry plasmid was generated in our previous study (Shen et al., 2022). The different mClover3-tagged DDX3X variants were generated using fusion PCR with the wild-type DDX3X-mCherry plasmid as template. For the APEX2-MS experiments, the DNA fragment encoding APEX2 was PCR amplified from pcDNA5/FRT/TO APEX2-GFP (Addgene) and fused to the N-terminus of DDX3X using fusion PCR. To verify the specificity of APEX2 labeling, TRIM32 and ANKRD52 genes were cloned from HeLa cDNA, fused with a mCherry tag at the C terminus, and inserted into the pcDNA3 vector for mammalian cell expression. G3BP1 was also cloned from HeLa cDNA, fused with an mCherry tag at the C-terminus, and inserted into the pPB vector. All plasmids were validated by Sanger sequencing.

Protein purification

Wild-type and variant DDX3X tagged with mCherry were purified according to our previous report (Shen et al., 2022). Briefly, the plasmids were transformed into *Escherichia coli* strain BL21-RIL to express the recombinant proteins. The bacteria were cultured in lysogeny broth at 37°C until $OD_{600\ nm}$ = 0.8 before administration of 1 mM IPTG and shaken at 200 rpm at 16°C for 16 hrs after induction. The pellets from 2 L bacterial culture were resuspended with 80 mL binding buffer (25 mM Tris-HCl, pH 7.5, 10% glycerol, 500 mM NaCl) and subjected to sonication. After centrifuging at 12,000 rpm for 30 min to remove the cell debris, the supernatant was loaded onto a Ni-NTA column. Next, 10 column volumes of the binding buffer supplemented with 50 mM imidazole was used to wash away the non-specifically bound proteins. Another 10 column volumes of a high salt buffer (25 mM Tris-HCl, pH 7.5, 10% glycerol, and 2 M NaCl) was used to remove the associated RNAs from wild-type DDX3X and DDX3X variants. Finally, four column volumes of the binding buffer supplemented with 500 mM imidazole was used to elute the bound proteins, which were dialyzed into the storage buffer (25 mM Tris-HCl, pH 7.5, 500 mM NaCl, 10% glycerol, and 2 mM DTT) with TEV enzyme cleavage of the His-tag simultaneously for 1 hr at room temperature. Then, the proteins were concentrated using Amicon Ultra-15 (Millipore) tubes before loading to a Superdex 75 column, with storage buffer (25 mM Tris-HCl, pH 7.5, 500 mM NaCl, 10% glycerol, and 2 mM DTT). The purity of the proteins was analyzed by SDS-PAGE. Purified proteins were aliquoted, snap-frozen in liquid nitrogen, and stored at -80 °C. Once thawed, aliquots were never refrozen. All purification steps after sonication were performed at room temperature.

Electrophoretic mobility shift assay (EMSA)

To measure the RNA binding affinities of different DDX3X variants, EMSAs were carried out. A double-stranded RNA probe with 5' overhang, to which DDX3X is known to bind[19,31], with following sequences: 5'-biotin/ACCGCUGCCGUCGCUCCG/AlexF647N/-3' and 5'-/Cy3/UUUUUUUUUUUUUUUUUUUUUUUUUUUUUUUUUUUUUUUUUUUUUUUUUUUUUUUUUCGGAGCGACGGCAGCGGU-3' was used. Both strands were ordered from IDT and annealed by heating the equimolar mixtures of both strands at 65°C for 5 min, then slowly cooling the sample to room temperature over 3 hrs. Various concentrations of each mCherry-tagged DDX3X variant proteins were incubated with 100 nM double-stranded RNA probe at room for 30 min in a buffer consisting

of 50 mM Tris-HCl pH 7.5, 150 mM KCl, 2 mM $MgCl_2$, 10 mM beta-mercaptoethanol and .1 mg/mL BSA before loading to a homemade 6% polyacrylamide gel (37.5:1) in 0.5 × TBE buffer. The gel was run at 120 V for 2 hrs at 4°C. The gel was then scanned using an Amersham Typhoon using the Cy5 channel. Fiji was used to quantify intensity of the bottom free RNA band. Fraction bound was calculated using the following equation: Fraction bound = $100*(1-(I_n/I_o))$, where "I_n" is the intensity of the free probe band at a given concentration and "I_o" is the intensity of the free probe band at 0 nM protein. Fraction bound was plotted versus concentration in GraphPad Prism and fit with the Hill equation to give K_D.

Fluorescence imaging

HeLa cells were seeded to a 6-well plate with a coverslip in each well and cultured overnight. The various DDX3X plasmids were transfected to cells with Lipofectamine 2000 the next morning. After 24 hrs in culture, the cells were washed once with PBS and then fixed using 4% paraformaldehyde in PBST (PBS with 0.01% Tween-20) at room temperature for 15 min. Then, the cells were washed twice by PBST and permeabilized by 0.5% Triton in PBST at room temperature for 20 min. After being washed once with PBST, the cells were blocked with 1% BSA in PBST at room temperature for 30 min. After being washed three times with PBST, the cells were incubated with 0.5 µg/mL DAPI for 1 min. After 4 PBST washes, an antifade reagent (Invitrogen) was used to mount the slides. The images were taken using a Leica TCS SP8 confocal microscope.

Quantification of hollow puncta

To quantify the percentage of cells showing hollow puncta, a slide with HeLa cells transiently transfected with each DDX3X variant was scanned left to right and top to bottom. The images for the first 25 transfected cells with puncta were taken. We then calculated the number of cells with hollow puncta divided by the total 25 cells. For each DDX3X variant, three biological replicates were carried out. The results were plotted using GraphPad Prism.

EU labeling of RNA in cells

To quantify the RNAs in DDX3X variant condensates, the cellular RNAs were first labeled with 5-ethynyl uridine (EU). An Alexa Fluor 594 fluorophore was then added through a click chemistry reaction using Click-iT RNA image kits (ThermoFisher). Briefly, HeLa cells were seeded to a 6-well plate. The plasmids of DDX3X variants were transfected into the cells using Lipofectamine 2000. After 24 hrs in culture, the medium was removed and fresh medium containing 1 mM EU was added. After a 1 hr incubation, the cells were fixed and permeabilized as stated above. Alexa 594 was conjugated to EU using the Click-iT reaction. After three PBST washes, the cells were incubated with 1 mL Hoechst 33342 to stain the DNA. After 4 PBST washes, an antifade reagent (Invitrogen) was used to mount the slides. The images were taken using a Leica TCS SP8 confocal microscope. The average Alexa 594 intensity in hollow puncta of each DDX3X variant was quantified using Fiji [45], with the average Alexa 594 intensity in the corresponding nucleoplasm used for normalization.

Fluorescence recovery after photobleaching (FRAP)

The FRAP assays were conducted using the bleaching module of a Zeiss LSM 880 confocal microscope. The 488 nm laser was used to bleach the mClover3 signal, and the 561 nm laser was used to bleach the mCherry signal. HeLa cells were seeded on 35 mm poly-D-lysine coated glass-bottomed dishes (Mattek), and the plasmids of DDX3X variants were transfected into the HeLa cells. After 24 hrs culture, the normal DMEM medium was replaced with FluoroBrite DMEM (GIBCO) medium with 10% FBS. For full bleaching assay to dissect the molecule exchange between puncta and surroundings, an entire punctum was selected to bleach with 100% laser power and time-lapse images were collected afterward. To probe the molecule exchange inside

of the puncta, partial bleaching was performed by focusing on a circular region of interest (ROI) of a punctum using 100% laser power, and time-lapse images were collected afterward as well. The fluorescence intensity was directly measured in the Zen software. The values were reported relative to pre-bleaching time points. GraphPad Prism was used to plot the data. The halftime for each replicate was calculated using the following formula: $y=a\bullet(1-\exp(-b\bullet x)) + c$, in which "a" is the slow recovery fraction, "c" is the rapid diffusion fraction, and "b" is the recovery rate. The halftime is ln2 / b, and the mobile fraction is a + c. Significance was calculated using an unpaired Student's two-tailed t test.

Malachite green ATPase assay

ATPase measurements were taken using the Malachite Green Phosphate Assay Kit (Sigma) according to the manufacturer's instructions. Briefly, 1 μM of each mCherry tagged DDX3X variant protein was incubated with 100 ng/μL total RNA extracted from HeLa cells for 15 min in the reaction buffer (25 mM Tris-HCl, pH 8, 200 mM NaCl, 1 mM DTT, and 2 mM $MgCl_2$) before the addition of 2 mM ATP. The reaction was incubated at 16°C for 30 min. Then the reaction was quenched by the addition of malachite green mixture and left for an additional 30 min to develop the color. The samples were then loaded into a clear-bottom 384-well plate and the absorbance at OD_{620} nm was measured. Values were converted from absorbance units to μM free phosphate using a standard curve generated with the kit's phosphate standard. Background values (free phosphate detected from reactions lacking RNA) were subtracted from the values from reactions with RNA. Data were plotted in GraphPad Prism. Significance was calculated using an unpaired Student's two-tailed t test.

Cellular APEX labeling

To capture the proteins in the hollow puncta formed by R475G DDX3X, a recently established proximity labeling method was carried out followed by mass spectrometry[19,32]. Briefly, one 10 cm plate of HEK 293T cells was transfected with 3.5 μg APEX2 fused wild-type DDX3X- or R475G-expressing plasmid. After 24 hrs culture, the normal DMEM medium was replaced with DMEM medium supplemented with 500 mM biotin-phenol for 30 min. Then, H_2O_2 (Sigma-Aldrich) was added to each cell culture dish at 1 mM final concentration for exactly 1 min with gentle agitation. To stop the labeling, the culture medium was removed, and the quenching solution (10 mM sodium ascorbate, 10 mM sodium azide, and 5 mM Trolox in PBS) was immediately used to wash the cells three times. Finally, 1 mL quenching solution was applied to cover the cells. Cells were then collected with a cell scraper. The unlabeled control samples were prepared in parallel under the same procedure as aforementioned, without the addition of the H_2O_2.

Mass spectrometry sample preparation

The cell pellets collected after APEX labeling were lysed by gentle pipetting in RIPA buffer (50 mM Tris-HCl pH 7.5, 150 mM NaCl, 0.1% (wt/vol) SDS, 0.5% (wt/vol) sodium deoxycholate and 1% (vol/vol) Triton X-100) supplemented with 1x protease inhibitor cocktail, 1 mM PMSF and quenchers (10 mM sodium azide, 10 mM sodium ascorbate and 5 mM Trolox). After resuspension and on ice for ~ 2 min, the lysates were clarified by centrifuging at 15,000 g for 10 min at 4 °C. The concentration of the cell lysate was quantified by using the Pierce 660-nm assay. The same amount of cell lysate was incubated with RIPA buffer washed Pierce Streptavidin magnetic beads for 1 hr at room temperature on a rotator. The beads were pelleted using a magnetic rack and washed sequentially with 1 mL RIPA buffer twice, once with 1 M KCl, once with 0.1 M Na_2CO_3, once with 2 M urea in 10 mM Tris-HCl, pH 8.0, and twice with RIPA lysis buffer. The wash buffers were kept on ice throughout the procedure. The biotinylated proteins were eluted from the beads by boiling each sample in 30 μL of 3 × protein loading buffer supplemented with 2 mM biotin and 20 mM DTT for 10 min. Then, placed the samples on a magnetic rack to pellet the beads and to collect the eluate. All the eluate was loaded to 10% SDS-PAGE gel and ran 1 cm into the gel.

Then, the entire stained gel regions were excised, reduced with tris(2-carboxyethyl)phosphine (TCEP), alkylated with iodoacetamide, and digested with trypsin. Tryptic digests were analyzed using a 95 min LC gradient on the Thermo Q Exactive HF mass spectrometer as described previously [46].

Mass spectrometry data analysis

MS/MS data were searched with full tryptic specificity against the Swiss Prot human proteome database (06/04/2021), the wild-type DDX3X and R475G protein sequences, and a common contaminant database using MaxQuant 1.6.17.0[47]. Search parameters used include two missed cleavages, static carbamidomethylation of Cys, and variable modifications of protein N-terminal acetylation, Asn deamidation, and Met oxidation. Consensus identification lists were generated with false discovery rates set at 1% for protein, and peptide identifications. High confidence identification of proteins with significant change refers to proteins satisfying the following criteria: minimum fold-change of 2 in either direction, adjusted p-value < 0.1, identified by a minimum of 2 razor + unique peptides, and detected in at least two of the three replicates. High confidence proteins were subjected to the gene ontology (GO) analysis using the Metascape [48].

Protein quantification and western blot

Protein concentrations of the samples were calculated using the Bradford Assay (Thermo Fisher, 23246). Protein samples were boiled at 95°C in Laemmli sample buffer for 10 min. After brief centrifugation, the samples were loaded onto SDS-PAGE gels. After running at 180 V for 1 hr, the gels were transferred to membrane by semi-dry transfer apparatus at 20 V for 50 min. Then, the membrane was blocked with 5% milk or BSA in 1 × PBST for 30 mins at room temperature or 4°C overnight. The membrane was then incubated in 3% milk or BSA in 1 × PBST containing the corresponding primary antibody overnight at 4°C. After washing three times with 1 × PBST, the horseradish peroxidase (HRP)-conjugated secondary antibody (1:20,000) in 1% of milk was applied and incubated at room temperature for 1 hr. After washing three times with PBST, the membranes were visualized using ECL Western Blotting Detection Kit (Thermo Fisher).

QUANTIFICATION AND STATISTICAL ANALYSIS

Images were analyzed using Fiji. All data are presented as the mean ± standard error of mean (s.e.m.) or standard deviation (s.d.) from the independent determinations. The statistical analyses were performed using the GraphPad Prism (GraphPad Software, Inc,; La Jolla, CA, USA). Differences of means were tested for statistical significance with unpaired two-tailed Student's t-test. *p < 0.05; **p < 0.01; ***p < 0.001; ****p < 0.0001; n.s. means p > 0.05.

Supplemental Table

Supplemental Table1, Summary of WT-DDX3X and R475G APEX2 pull-down proteomics results.

References

1. Mo, J. *et al.* DDX3X: structure, physiologic functions and cancer. *Mol. Cancer* **20,** 38 (2021).
2. Sharma, D. & Jankowsky, E. The Ded1/DDX3 subfamily of DEAD-box RNA helicases. *Crit Rev Biochem Mol Biol* **49,** 343–360 (2014).
3. Chen, C.-Y. *et al.* Targeted inactivation of murine Ddx3x: essential roles of Ddx3x in placentation and embryogenesis. *Hum. Mol. Genet.* **25,** 2905–2922 (2016).
4. Lennox, A. L. *et al.* Pathogenic DDX3X Mutations Impair RNA Metabolism and Neurogenesis during Fetal Cortical Development. *Neuron* **106,** 404–420.e8 (2020).
5. Singleton, M. R., Dillingham, M. S. & Wigley, D. B. Structure and mechanism of helicases and nucleic acid translocases. *Annu. Rev. Biochem.* **76,** 23–50 (2007).
6. Calviello, L. *et al.* DDX3 depletion represses translation of mRNAs with complex 5' UTRs. *Nucleic Acids Res.* **49,** 5336–5350 (2021).
7. Shih, J.-W. *et al.* Critical roles of RNA helicase DDX3 and its interactions with eIF4E/PABP1 in stress granule assembly and stress response. *Biochem. J.* **441,** 119–129 (2012).
8. Jones, D. T. W. *et al.* Dissecting the genomic complexity underlying medulloblastoma. *Nature* **488,** 100–105 (2012).
9. Patmore, D. M. *et al.* DDX3X suppresses the susceptibility of hindbrain lineages to medulloblastoma. *Dev. Cell* **54,** 455–470.e5 (2020).
10. Valentin-Vega, Y. A. *et al.* Cancer-associated DDX3X mutations drive stress granule assembly and impair global translation. *Sci. Rep.* **6,** 25996 (2016).
11. Gong, C. *et al.* Sequential inverse dysregulation of the RNA helicases DDX3X and DDX3Y facilitates MYC-driven lymphomagenesis. *Mol. Cell* **81,** 4059–4075.e11 (2021).
12. Jiang, L. *et al.* Exome sequencing identifies somatic mutations of DDX3X in natural killer/T-cell lymphoma. *Nat. Genet.* **47,** 1061–1066 (2015).
13. Ojha, J. *et al.* Identification of recurrent truncated DDX3X mutations in chronic lymphocytic leukaemia. *Br. J. Haematol.* **169,** 445–448 (2015).
14. Takahashi, K. *et al.* Clinical implications of cancer gene mutations in patients with chronic lymphocytic leukemia treated with lenalidomide. *Blood* **131,** 1820–1832 (2018).
15. Epling, L. B., Grace, C. R., Lowe, B. R., Partridge, J. F. & Enemark, E. J. Cancer-associated mutants of RNA helicase DDX3X are defective in RNA-stimulated ATP hydrolysis. *J. Mol. Biol.* **427,** 1779–1796 (2015).
16. Weil, M. D., Lamborn, K., Edwards, M. S. & Wara, W. M. Influence of a child's sex on medulloblastoma outcome. *JAMA* **279,** 1474–1476 (1998).
17. Nguyen, T. A. *et al.* A Cluster of Autism-Associated Variants on X-Linked NLGN4X Functionally Resemble NLGN4Y. *Neuron* **106,** 759–768.e7 (2020).
18. Shi, B. *et al.* UTX condensation underlies its tumour-suppressive activity. *Nature* **597,** 726–731 (2021).
19. Shen, H. *et al.* Sexually dimorphic RNA helicases DDX3X and DDX3Y differentially regulate RNA metabolism through phase separation. *Mol. Cell* **82,** 2588–2603.e9 (2022).
20. Godfrey, A. K. *et al.* Quantitative analysis of Y-Chromosome gene expression across 36 human tissues. *Genome Res.* **30,** 860–873 (2020).
21. Hu, H. *et al.* X-exome sequencing of 405 unresolved families identifies seven novel intellectual disability genes. *Mol. Psychiatry* **21,** 133–148 (2016).
22. Snijders Blok, L. *et al.* Mutations in DDX3X Are a Common Cause of Unexplained Intellectual Disability with Gender-Specific Effects on Wnt Signaling. *Am. J. Hum. Genet.* **97,** 343–352 (2015).
23. Markmiller, S. *et al.* Context-Dependent and Disease-Specific Diversity in Protein Interactions within Stress Granules. *Cell* **172,** 590–604.e13 (2018).
24. Hondele, M. *et al.* DEAD-box ATPases are global regulators of phase-separated

organelles. *Nature* **573,** 144–148 (2019).
25. Floor, S. N., Condon, K. J., Sharma, D., Jankowsky, E. & Doudna, J. A. Autoinhibitory Interdomain Interactions and Subfamily-specific Extensions Redefine the Catalytic Core of the Human DEAD-box Protein DDX3. *J. Biol. Chem.* **291,** 2412–2421 (2016).
26. Sengoku, T., Nureki, O., Nakamura, A., Kobayashi, S. & Yokoyama, S. Structural basis for RNA unwinding by the DEAD-box protein Drosophila Vasa. *Cell* **125,** 287–300 (2006).
27. Song, H. & Ji, X. The mechanism of RNA duplex recognition and unwinding by DEAD-box helicase DDX3X. *Nat. Commun.* **10,** 3085 (2019).
28. Alberti, S., Gladfelter, A. & Mittag, T. Considerations and Challenges in Studying Liquid-Liquid Phase Separation and Biomolecular Condensates. *Cell* **176,** 419–434 (2019).
29. Schmidt, H. B. & Rohatgi, R. In Vivo Formation of Vacuolated Multi-phase Compartments Lacking Membranes. *Cell Rep.* **16,** 1228–1236 (2016).
30. Niaki, A. G. *et al.* Loss of Dynamic RNA Interaction and Aberrant Phase Separation Induced by Two Distinct Types of ALS/FTD-Linked FUS Mutations. *Mol. Cell* **77,** 82–94.e4 (2020).
31. Kim, Y. & Myong, S. RNA remodeling activity of DEAD box proteins tuned by protein concentration, RNA length, and ATP. *Mol. Cell* **63,** 865–876 (2016).
32. Fazal, F. M. *et al.* Atlas of Subcellular RNA Localization Revealed by APEX-Seq. *Cell* **178,** 473–490.e26 (2019).
33. Marmor-Kollet, H. *et al.* Spatiotemporal proteomic analysis of stress granule disassembly using APEX reveals regulation by sumoylation and links to ALS pathogenesis. *Mol. Cell* **80,** 876–891.e6 (2020).
34. Padrón, A., Iwasaki, S. & Ingolia, N. T. Proximity RNA Labeling by APEX-Seq Reveals the Organization of Translation Initiation Complexes and Repressive RNA Granules. *Mol. Cell* **75,** 875–887.e5 (2019).
35. Yu, H. *et al.* HSP70 chaperones RNA-free TDP-43 into anisotropic intranuclear liquid spherical shells. *Science* **371,** (2021).
36. Kellaris, G. *et al.* A hypomorphic inherited pathogenic variant in DDX3X causes male intellectual disability with additional neurodevelopmental and neurodegenerative features. *Hum. Genomics* **12,** 11 (2018).
37. Venkataramanan, S., Gadek, M., Calviello, L., Wilkins, K. & Floor, S. N. DDX3X and DDX3Y are redundant in protein synthesis. *RNA* **27,** 1577–1588 (2021).
38. Boehning, M. *et al.* RNA polymerase II clustering through carboxy-terminal domain phase separation. *Nat. Struct. Mol. Biol.* **25,** 833–840 (2018).
39. Su, X. *et al.* Phase separation of signaling molecules promotes T cell receptor signal transduction. *Science* **352,** 595–599 (2016).
40. Yang, P. *et al.* G3BP1 Is a Tunable Switch that Triggers Phase Separation to Assemble Stress Granules. *Cell* **181,** 325–345.e28 (2020).
41. Feric, M. *et al.* Coexisting liquid phases underlie nucleolar subcompartments. *Cell* **165,** 1686–1697 (2016).
42. Alshareedah, I., Moosa, M. M., Raju, M., Potoyan, D. A. & Banerjee, P. R. Phase transition of RNA-protein complexes into ordered hollow condensates. *Proc. Natl. Acad. Sci. USA* **117,** 15650–15658 (2020).
43. Nicklas, S. *et al.* A complex of the ubiquitin ligase TRIM32 and the deubiquitinase USP7 balances the level of c-Myc ubiquitination and thereby determines neural stem cell fate specification. *Cell Death Differ.* **26,** 728–740 (2019).
44. Mack, N. A., Whalley, H. J., Castillo-Lluva, S. & Malliri, A. The diverse roles of Rac signaling in tumorigenesis. *Cell Cycle* **10,** 1571–1581 (2011).
45. Schindelin, J. *et al.* Fiji: an open-source platform for biological-image analysis. *Nat. Methods* **9,** 676–682 (2012).
46. Yan, Q. *et al.* Proximity labeling identifies a repertoire of site-specific R-loop modulators.

Nat. Commun. **13,** 53 (2022).
47. Cox, J. & Mann, M. MaxQuant enables high peptide identification rates, individualized p.p.b.-range mass accuracies and proteome-wide protein quantification. *Nat. Biotechnol.* **26,** 1367–1372 (2008).
48. Zhou, Y. *et al.* Metascape provides a biologist-oriented resource for the analysis of systems-level datasets. *Nat. Commun.* **10,** 1523 (2019).